Applied Mathematical Modelling 142 (2025) 115966

Contents lists available at ScienceDirect

Applied Mathematical Modelling

journal homepage: www.elsevier.com/locate/apm

Dissolution of variable-in-shape drug particles via the level-set method

Emiliano Cristiani [a], Mario Grassi [b,*], Francesca L. Ignoto [a,c], Giuseppe Pontrelli [a]

[a] Istituto per le Applicazioni del Calcolo, Consiglio Nazionale delle Ricerche, Rome, Italy
[b] Dipartimento di Ingegneria e Architettura, Università di Trieste, Trieste, Italy
[c] Dipartimento di Scienze di Base e Applicate per l'Ingegneria, Sapienza Università di Roma, Rome, Italy

ARTICLE INFO

Keywords:
Drug dissolution
Variable shape particles
Recrystallization
Solubility
Wettability
Mathematical modeling
Level-set method
Hamilton-Jacobi equations

ABSTRACT

In this work, we deal with a mathematical model describing the dissolution process of irregularly shaped particles. In particular, we consider a complete dissolution model accounting for surface kinetics, convective diffusion, and relative velocity between fluid and dissolving particles, for three drugs with different solubility and wettability: theophylline, griseofulvin, and nimesulide. The possible subsequent recrystallization process in the bulk fluid is also considered. The governing differential equations are revisited in the context of the level-set method and Hamilton-Jacobi equations, then they are solved numerically. This choice allows us to deal with the simultaneous dissolution of hundreds of different polydisperse particles. We show the results of many computer simulations which investigate the impact of the particle size, shape, area/volume ratio, and the dependence of the interfacial mass transport coefficient on the surface curvature.

1. Introduction

The dissolution of a solid (drug) in a liquid phase can be defined as "the mixing of two phases (the solid and the liquid one) with the formation of a new homogeneous phase (i.e., the solution)" [1]. Thus, dissolution implies the destroying of the original crystalline network and the subsequent delivery of "solid" atoms/molecules in the liquid phase. Kinetically speaking, it can be considered as the combination of five concurrent steps [1–3], comprising:

1. the contact of the liquid with the solid surface (wetting), giving origin to the formation of a new solid-liquid interface starting from the solid-vapor one;
2. the breakdown of the crystalline network (fusion);
3. the transfer of solid molecules to the solid-liquid interface (solvation);
4. the diffusion of the solvated molecules through the unstirred boundary layer surrounding the solid surface (diffusion);
5. the convective transport of solvated drug molecules into the well stirred bulk solution (convection).

---

[*] Corresponding author.
E-mail address: mario.grassi@dia.units.it (M. Grassi).

https://doi.org/10.1016/j.apm.2025.115966
Received 11 July 2024; Received in revised form 9 January 2025; Accepted 20 January 2025

Available online 27 January 2025
0307-904X/© 2025 The Author(s). Published by Elsevier Inc. This is an open access article under the CC BY-NC-ND license (http://creativecommons.org/licenses/by-nc-nd/4.0/).

As each one of the first four steps implies to overcome an energetic barrier, the sum of these energies represents the total resistance to solid (drug) dissolution. Obviously, the higher the dissolution energy required (i.e., the higher the mass transfer resistance) the slower the dissolution kinetics is.

The analysis of the dissolution phenomenon is not only scientifically interesting *per se*, but it is absolutely relevant for the pharmaceutical field. In fact, it affects the bioavailability of drugs, i.e., the rate and extent to which the drug is absorbed from a delivery system and becomes available at the site of drug action [4,5]. Bioavailability depends on both the drug permeability through the cell membrane and on the drug dissolution in physiological fluids, as solid drugs cannot be absorbed by living tissues [4]. This last aspect is very important remembering that about 40% of the market drugs and 70 – 90% of new chemical entities are characterized by low dissolution kinetics due to their poor water solubility [6–9]. Accordingly, scientific and industrial reasons have attracted the attention of many researchers on dissolution since long ago. The seminal work of Hixson and Crowell [10–12], who, for the first time, considered the effect of surface reduction upon the dissolution of spherical particles and established the well-known cubic law, dates back to 1931. Later on, Niebergall et al. [13] noted a deviation from the cubic law and proposed an improvement assuming that the thickness of the diffusion layer surrounding the dissolving particle was proportional to the square root of the mean particle diameter. The elegant approach of Pedersen and coworkers extended the mathematical modeling of dissolution to polydisperse spherical particles [14–17]. Notably, this model reduces to the Hixson-Crowell model in the case of monodisperse systems. Other authors argued that the overall dissolution process can be affected by the occurrence of a surface reaction between solute and solvent molecules or by limited solid surface solubility [18]. In either case, the final result is a time-dependent drug concentration at the solid-liquid interface that is lower than the drug solubility in the solvent. A similar phenomenon concerns metastable solids undergoing a phase change (amorphous-crystalline or polymorphic transformation) upon dissolution, this reflecting in a time-dependent solid drug solubility [19,20]. Interestingly, the possible drug degradation in the bulk fluid after dissolution was also considered [21].

Another aspect that attracted the interest of researchers was the effect of particles shape on dissolution [22]. While Hirai et al. [23] did not explicitly consider the shape of the particles but focused instead on a law which can describe the time dependence of the dissolution surface, Abrami et al. [20] dealt with spherical, cylindrical and parallelepiped particles, Hsu and Wu [24] considered spheres, cylinders, bi-cones, cones and inverse-cones shaped particles, and Yuan et al. [25] focused on the dissolution of irregularly shaped particles. It is easy to predict that the symbiotic-synergic effect occurring between these (and other) theoretical models and the emerging experimental set up aimed to visualize particle shape variation upon dissolution [20,26] will soon lead to important new achievements in this field.

Undoubtedly, particle shape is also connected with two other important aspects, i.e. drug concentration profile in the boundary layer (BL) surrounding the solid surface, and BL thickness. Indeed, drug concentration profile is not linear, as originally assumed [2,27–29], unless dissolution occurs from a flat surface. In addition, BL thickness depends on both dissolution medium hydrodynamic conditions and on particle dimension, as nicely documented by D'Arcy and Persoons [30,31]. Very recently, Assunção et al. [32,33], demonstrated the possibility of getting nonspherical particles from the dissolution of initially spherical particles.

To the best of our knowledge, one of the most recent and comprehensive mathematical model accounting for many aspects connected to dissolution and presented in this introduction is that by Abrami et al. [34] who employed the concept of local curvature radius to describe the dissolution of concave and convex surfaces of any shape. The target of this work is to move forward, developing a mathematical model capable to account also for the simultaneous presence of solid particles with different shapes and dimensions, this being one of the most common situation met in real conditions. Moreover, the effect of particles surface/volume ratio (or perimeter/surface ratio in the two dimensional case), and the curvature radius dependence of the interfacial mass transport coefficient will be considered. To this purpose, our simulations dealt with three widely used drugs, namely *theophylline* (soluble and wettable-bronco-dilatator drug), *griseofulvin* (poorly soluble but wettable-antifungal drug) and *nimesulide* (poorly soluble and poorly wettable-non-steroidal anti-inflammatory drug).

The mathematical model of the dissolution dynamics is revisited in the context of the level-set method and Hamilton–Jacobi equations [35], which was found to be very useful and versatile as it allows to manage hundreds of particles with a reasonable computational effort (computing the solution requires some minutes). Moreover, it allows to easily manage the presence of "corners" in the particles shape. All the simulations were performed in two dimensions but the extension to three dimensions is also possible.

2. Modeling drug dissolution

As discussed in Sect. 1, dissolution is a complex process made up of a series of different sub-phenomena, each one representing an energetic barrier. Accordingly, the inverse of the overall dissolution resistance equals the sum of the resistance inverse competing to each sub-phenomenon [1]. The aim of this section is to translate into mathematical terms the above mentioned sub-phenomena in order to get a model able to describe the time variation of drug concentration inside the release environment.

In this paper we overcome the usual assumption of particles of spherical shape in the attempt to understand the effect of the local curvature on the dissolution process. Since particles change their shape and size during dissolution, this reflects in a change of dissolution rate over time.

Let us consider a particle P_0 of arbitrary shape in $\mathbb{R}^3$ with initial volume V_0, enclosed by a surface S_0. The particle dissolves in an external bulk fluid of constant volume $V_{\text{EXT}} \gg V_0$. In the following, we will denote by $V^+ = V_{\text{EXT}}/V_0$ the ratio between the two volumes. Moreover, an interaction between the solute and solvent (solvation) at solid-liquid interface yields the formation of a BL of thickness δ surrounding the solid surface [34]. During dissolution, the surface evolves and the volume reduces accordingly. In the following we will denote by $P(t)$ the dissolving particle at time t, by $V(t)$ its volume, and by $S(t)$ its external surface, see Fig. 1.

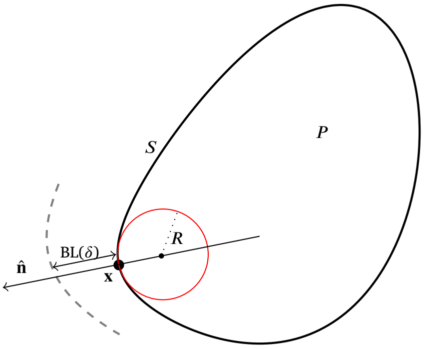

Fig. 1. Two-dimensional representation of a particle P dissolving in the bulk fluid, with osculating circle of radius R at a generic point $\mathbf{x}$ on its surface S. Local dissolution occurs in normal direction with respect to S.

To evaluate the amount of drug dissolved, the mass balance principle is used. By considering an infinitesimal part of the surface $dS(\mathbf{x})$ in a neighborhood of the point $\mathbf{x} \in S$,[1] the corresponding loss of mass equals the drug flux leaving dS [34]:

$$\frac{dM_b}{dt} = -\frac{dM_s}{dt} = \int_S K(\mathbf{x})(C_s - C_b)dS, \tag{1}$$

where M_s is the particle mass, M_b is the drug mass in the bulk fluid, C_b is the concentration of the bulk fluid, and $K(\mathbf{x})$ is the position-dependent mass transfer coefficient (see dedicated Sect. 3 later on) [20,34]. Eq. (1) states that in the neighborhood of $\mathbf{x}$ the solid mass reduces by $K(\mathbf{x})(C_s - C_b)dS$ in the unit time and, correspondingly, the same amount is transferred into the fluid. In other words, (1) shows that the dissolution rate is position-dependent, with the implicit assumption that dissolution at $\mathbf{x}$ occurs in the *normal direction* with respect to the surface.

In (1) the solubility $C_s(t)$ is an exponentially decreasing function of time, as a consequence of a possible drug phase transformation at the solid-liquid interface [36]:

$$C_s(t) = C_{sf} + (C_{s0} - C_{sf})\exp(-k_r t), \tag{2}$$

where C_{s0} and C_{sf} ($C_{s0} \geq C_{sf}$) are the initial and final values of drug solubility, respectively, and k_r is the surface recrystallization constant. Should $C_b(t)$ exceed $C_s(t)$, drug dissolution ends and drug recrystallization in the release environment starts. This phenomenon can be properly described by the well-known Nogami model [36]:

$$\frac{dM_c}{dt} = -k_{rb}V_{\text{EXT}}(C_s - C_b), \tag{3}$$

with M_c the recrystallized mass and k_{rb} the bulk recrystallization constant [36]. At every step of the process, the conservation of mass holds, that is:

$$M_0 = M_s(t) + C_b(t)V_{\text{EXT}} + M_c(t), \tag{4}$$

with M_0 the initial particle mass, and $C_b(t)V_{\text{EXT}}$ the drug mass dissolved in the bulk fluid. By time differentiating (4), we have

$$\frac{d}{dt}\left(M_s + C_bV_{\text{EXT}} + M_c\right) = 0, \tag{5}$$

and summing up the contributions given by (1),

$$V_{\text{EXT}}\frac{dC_b}{dt} + \frac{dM_c}{dt} = (C_s - C_b)\int_S K(\mathbf{x})dS \tag{6}$$

i.e.

$$\frac{dC_b}{dt} = \frac{(C_s - C_b)\displaystyle\int_S K(\mathbf{x})dS - \frac{dM_c}{dt}}{V_{\text{EXT}}}. \tag{7}$$

By virtue of (3), (7) is finally replaced by

$$\frac{dC_b}{dt} = \frac{C_s - C_b}{V_{\text{EXT}}}\int_S K(\mathbf{x})dS + k_{rb}(C_s - C_b). \tag{8}$$

---

[1] For the sake of simplicity, in the following we omit the dependence of the variables on $\mathbf{x}$ and t, unless required by the context.

The last equation says that the variation of concentration C_b is due in part to the dissolution of the solid (positive contribution) and in part to the recrystallization (negative contribution). Actually, dissolution and recrystallization are not simultaneous, and the whole process can be subdivided in two subsequent regimes:

1) Dissolution In the first phase, as long as $C_b < C_s$, only dissolution takes place, and C_b increases. Although, in principle, particles dissolution depends also on the liquid phase density and its variation with solid concentration as nicely documented by Assunção and coworkers [32,33], for the sake of simplicity we follow a more traditional approach neglecting this dependence. In this framework, the dissolution process is described by the following equations:

$$\begin{cases} \dfrac{d\mathbf{x}}{dt} = -\dfrac{K(\mathbf{x})}{\rho_s}(C_s - C_b)\hat{\mathbf{n}} \\ \dfrac{dC_b}{dt} = \dfrac{C_s - C_b}{V_{\text{EXT}}} \displaystyle\int_S K(\mathbf{x})dS \end{cases}, \qquad C_b < C_s, \tag{9}$$

where ρ_s is the particle density, and $\hat{\mathbf{n}}$ is the unit external normal (note the ODEs are nonlinear because of $K(\mathbf{x})$), and initial conditions

$$\mathbf{x}(0) = \mathbf{x}_0, \qquad C_b(0) = 0, \tag{10}$$

for any $\mathbf{x}_0 \in S_0$.

Remark 1 *(spherical particles).* Assuming that the liquid density and its variation with drug concentration do not affect solid dissolution (see the beginning of Section 2), we get that if P_0 is a sphere, the particle maintains its original shape during dissolution and the computation simplifies. Therefore, the dynamics of $P(t)$ can be described by the evolution of any point on its surface or, equivalently, of its radius R. Moreover, K is constant and (9)-(10) simplifies as:

$$\begin{cases} \dfrac{dR}{dt} = -\dfrac{K}{\rho_s}\left(C_s - C_b\right)\hat{\mathbf{n}} \\ \dfrac{dC_b}{dt} = 4\pi R^2 K \, \dfrac{C_s - C_b}{V_{\text{EXT}}} \end{cases}, \qquad C_b < C_s, \tag{11}$$

with

$$R(0) = R_0, \qquad C_b(0) = 0. \tag{12}$$

2) Recrystallization In the second step, which starts at the time t^* such that $C_b(t^*) = C_s(t^*)$, dissolution stops and, as long as $C_b \geq C_s$, the recrystallization phase takes place with a progressive reduction of C_b. This lasts until the time t_f such that the equivalence $C_b(t_f) = C_s(t_f)$ holds true for the second time. This process is governed by the following linear equations:

$$\begin{cases} \dfrac{dM_c}{dt} = -k_{rb}V_{\text{EXT}}(C_s - C_b) \\ \dfrac{d\mathbf{x}}{dt} = 0 \\ \dfrac{dC_b}{dt} = k_{rb}(C_s - C_b) \end{cases}, \qquad C_b \geq C_s, \tag{13}$$

with initial conditions:

$$M_c(t^*) = 0, \qquad C_b(t^*) = C_s(t^*). \tag{14}$$

Eqs. (13)-(14) admit the following analytical solution:

$$\begin{aligned} C_b(t) = {} & C_s(t^*)\exp(-k_{rb}(t - t^*)) + \\ & + (C_{s0} - C_{sf})\frac{k_{rb}}{k_{rb} - k_r}\exp(-k_{rb}t)\Big(\exp((k_{rb} - k_r)t) - \exp((k_{rb} - k_r)t^*)\Big) + \\ & + C_{sf}(1 - \exp(-k_{rb}(t - t^*))) \end{aligned} \tag{15}$$

and

$$\begin{aligned} \frac{M_c(t)}{V_{\text{EXT}}\,k_{rb}} = {} & -\frac{C_s(t^*)}{k_{rb}}\exp(k_{rb}t^*)\Big(\exp(-k_{rb}t) - \exp(-k_{rb}t^*)\Big) + \\ & + \frac{C_{s0} - C_{sf}}{k_r}\left(1 - \frac{k_{rb}}{k_{rb} - k_r}\right)\Big(\exp(-k_r t) - \exp(-k_r t^*)\Big) + \end{aligned}$$

$$+\frac{k_{rb}(C_{s0}-C_{sf})\exp((k_{rb}-k_r)t^*)+(k_{rb}-k_r)C_{sf}\exp(k_{rb}t^*)}{k_{rb}(k_{rb}-k_r)}\Big(\exp(-k_{rb}t)-\exp(-k_{rb}t^*)\Big). \tag{16}$$

3. The mass transfer coefficient K

As discussed in [34], dissolution depends on solid wettability with respect to the dissolving fluid, on the surface curvature, and on the thickness of the BL, which – in turn – depends on the surface curvature and on the relative velocity between solid surface and fluid [30].

We assume that 1) dissolution occurs in the normal direction with respect to the solid surface, 2) mass transport inside the BL occurs according to a one-dimensional diffusive mechanism, and 3) pseudo-stationary conditions are rapidly reached in the BL.

The main simplifying assumption of our approach consists in supposing that drug transport inside the BL can be described by the one-dimensional (radial) form of Fick's second law in pseudo-stationary conditions implying $\partial C/\partial t \approx 0$, where C is the space-dependent drug concentration in BL. In doing so, the dissolution process is only affected by the solid density (ρ_s). If transient conditions were considered in mass transport ($\partial C/\partial t \neq 0$), also liquid density and its variation with solid concentration would play an important role in dissolution as documented in [32,33].

Under our assumptions it can be demonstrated that overall mass transfer coefficient K is given by

$$K=\frac{\frac{1}{\sigma}}{\frac{1}{k_d}+\frac{\sigma}{k_m}}=\left[\sigma\left(\frac{1}{k_d}+\frac{\sigma}{k_m}\right)\right]^{-1} \tag{17}$$

where k_d is the hydrodynamic mass transfer coefficient, connected to the BL local thickness, k_m is the interfacial mass transfer coefficient, and σ denotes the ratio between the maximum and minimum bounds of the BL. For further details the reader is referred to [20].

Curvature radius It is well known that at any point $\mathbf{x}$ of a surface S one can define two principal curvatures κ_1 and κ_2, defined as the maximum and minimum of the curvature of a curve contained in the surface and passing through the point $\mathbf{x}$. With these curvatures, one can then define the *mean curvature* $\kappa_M=(\kappa_1+\kappa_2)/2$. For our purposes, we define a suitable indicator of the curvature radius at any point $\mathbf{x}$ of the surface as:

$$R=\frac{1}{\kappa_M}.$$

Note that, in 2D, the curvature κ is uniquely defined, and $R=\frac{1}{\kappa}$ corresponds to the radius of the osculating circle, see Fig. 1. As a consequence, σ in (17) can be written as a function of R, as

$$\sigma=\frac{R+\delta}{R}=1+\frac{\delta}{R}=1+\frac{D}{k_d\,R}, \tag{18}$$

where we have used the known relation $k_d=D/\delta$ [37].

In previous papers it has been shown, by experimental evidence, that the hydrodynamic mass transfer (or intrinsic dissolution) k_d is inversely related to the radius for spherical particles [30]. Although some authors theoretically demonstrated the superiority of other approaches, see [32], following our previous works we consider the following equation for k_d [34,38]:

$$k_d=\frac{D}{2R}\left(2+0.6\sqrt{\frac{2R\,\Delta U}{\nu_f}}\left(\frac{\nu_f}{D}\right)^{1/3}\right), \tag{19}$$

where D is the drug diffusivity in the bulk fluid, ν_f is the kinematic viscosity, and

$$\Delta U=(\rho_s-\rho_f)g\frac{(2R_{\mathrm{EQ}})^2}{18\eta_f} \tag{20}$$

is the terminal relative velocity in non-accelerating fluid (with ρ_f the fluid density, η_f the fluid dynamic viscosity, g the gravity acceleration). That expression of ΔU is the result of the balance between drag and buoyancy force [30]. In (20), the time-dependent quantity R_{EQ} is defined as the radius of an *equivalent sphere* having the current particle volume

$$R_{\mathrm{EQ}}=\sqrt[3]{\frac{3V}{4\pi}}. \tag{21}$$

Note that, in the special case of a spherical particle, $R_{\mathrm{EQ}}(t)=R(t)$ at any time t. Note also, in (19)-(20), the nonlinear dependence of k_d on the particle size via R_{EQ}. It is important to remind that (20) represents just a raw estimation of ΔU, as it works only in steady state conditions. However, it is physically sound and, for practical purposes, it can be easily improved by the introduction of an adjustable parameter multiplying the solid-fluid density difference.

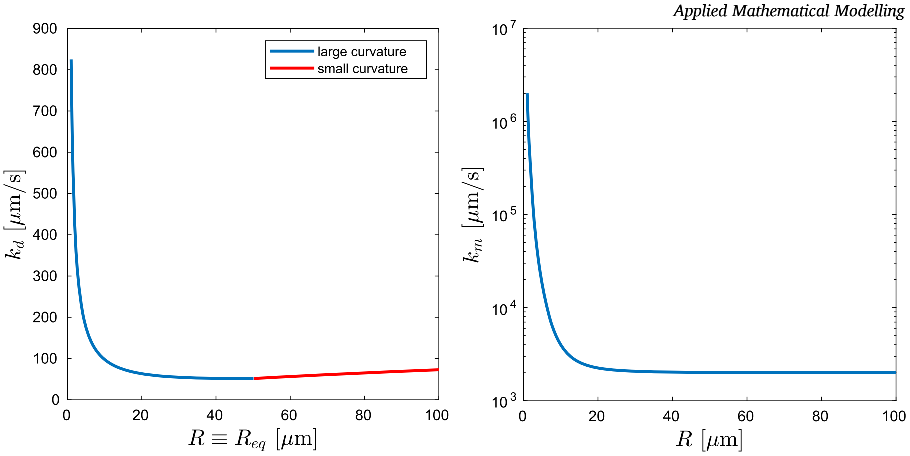

Fig. 2. Behavior of $k_d(R)$ (left) and $k_m(R)$ (right) for a spherical particle of theophylline 37 °C of initial radius 100 μm shrinking to 0 upon complete dissolution (other parameters in Table 1). Different colors highlight the switch between the two expressions of k_d (19) and (22).

For an almost flat surface ($R \to \infty$), (19) ceases to apply and we resort to the Levich approach [37]:

$$k_d = 0.621\ D^{2/3} \nu_f^{-1/6} \sqrt{\frac{\Delta U}{R_{\mathrm{EQ}}}}. \tag{22}$$

As (19) and (22) provide approximately the same k_d evaluation for sufficiently wide curvature radii, following the strategy proposed in [34], we define a limiting radius R_{PLANE} beyond which (22) replaces (19): R_{PLANE} is simply determined by equating the two equations and then solving for the unknown curvature radius, whose analytical solution reads:

$$R_{\mathrm{PLANE}} = \frac{\gamma_1}{2}\left(\frac{\gamma_1 + \sqrt{\gamma_1^2 + 4D\gamma_2}}{\gamma_2^2}\right) + \frac{D}{\gamma_2}, \tag{23}$$

$$\gamma_1 = 0.1 D^{2/3} \nu_f^{-1/6} \sqrt{\frac{4g(\rho_s - \rho_f)}{\eta_f}} R_{\mathrm{EQ}},$$

$$\gamma_2 = 0.207 D^{2/3} \nu_f^{-1/6} \sqrt{\frac{2g(\rho_s - \rho_f)}{\eta_f}} \sqrt{R_{\mathrm{EQ}}}.$$

Eq. (23) represents a simple strategy to manage the transition from a convex ($R \le R_{\mathrm{PLANE}}$) to a planar ($R > R_{\mathrm{PLANE}}$) dissolving surface. It is worth noting that R_{PLANE} depends on the particle size via R_{EQ}.

Regarding instead the interfacial mass transfer coefficient k_m, it depends on the local wetting properties of the dissolution surface. In this work we overcome the common hypothesis of a constant k_m, and adopt the following curvature-dependent expression:

$$k_m = k_m^{\infty}\left(\frac{\alpha}{R^3} + \frac{R}{R + 2d_T}\right), \tag{24}$$

where k_m^{∞} is the interfacial mass transfer coefficient associated with a planar surface ($R \to \infty$), d_T is the Tolman length, and α is a fitting parameter. Likewise k_d, k_m is also position-dependent via R. See Appendix C for the theoretical derivation of (24).

Fig. 2 shows the graphs of k_d and k_m as a function of R for a fully-dissolving spherical particle of initial radius $R_0 = 100$ μm. It is clear that both mass transfer coefficients increase for smaller R. However, while k_m is monotonic decreasing with R, k_d shows a minimum.

Fig. 3 shows the graphs of K as a function of R and R_{EQ} either in the general case and in the particular case of a spherical particle of initial radius $R_0 = 100$ μm. It is clear that the dependence of K on R is more similar to that of k_d rather than to that of k_m. This is simply due to the fact that the drug considered for these plots (theophylline) is a water wettable substance so that k_m is much higher than k_d. Obviously, for poorly water wettable drugs, the predominance of the k_m on K takes place. All these considerations make clear the complex relation occurring between K and R also for spherical particles where $R = R_{\mathrm{EQ}}$.

4. The level-set methodology

The level-set method was introduced in [35] and since then it was successfully applied in many contexts, see e.g., [39,40]. It allows Eulerian-tracking of the evolution of a $(d-1)$-dimensional surface S embedded in $\mathbb{R}^d$ and transported by a given velocity vector field $\mathbf{v}(t, \mathbf{x}; S)$ possibly dependent on time, space, and also on the shape of the surface itself. In our specific case, S is the boundary of the

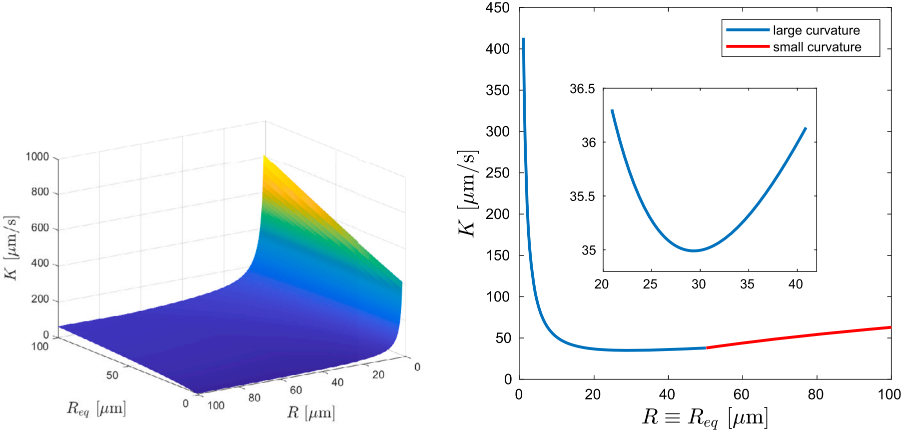

Fig. 3. Behavior of $K(R, R_{\mathrm{EQ}})$ (left) and $K(R, R_{\mathrm{EQ}} = R)$ (right, for a sphere) for a particle of theophylline 37 °C (other parameters in Table 1). Note that $K(R, R)$ is not monotone (see inset graph). Different colors highlight the switch between the two expressions of k_d (19) and (22).

drug particle P, and $\mathbf{v}$ controls its motion. Using the level-set method, every point $\mathbf{x}$ of the surface is moved according to the velocity field $\mathbf{v}(t, \mathbf{x})$. Note that the level-set approach does not perform a Lagrangian-tracking of every single point of the particle surface from the beginning to the end of its evolution, as it is done in [34].

Let us briefly recall the method in the case $d = 3$. The main idea of the level-set method stems from the definition of a level-set function $\varphi(\mathbf{x}, t) : \mathbb{R}^3 \times \mathbb{R}^+ \to \mathbb{R}$ such that

$$S(t) = \{\mathbf{x} : \varphi(\mathbf{x}, t) = 0\}, \quad \forall t \geq 0. \tag{25}$$

In this way the surface is recovered as the zero level set of φ at any time. Initially, the function φ is chosen in such a way that

$$\varphi(\mathbf{x}, 0) = \varphi_0(\mathbf{x}) \begin{cases} > 0, & \text{if } \mathbf{x} \notin \overline{P_0}, \\ = 0, & \text{if } \mathbf{x} \in S_0, \\ < 0, & \text{if } \mathbf{x} \in P_0. \end{cases} \tag{26}$$

A typical choice for $\varphi(\mathbf{x}, 0)$ is the signed distance function from S_0, although this choice does not lead to a smooth function. One can prove [40] that the level-set function φ satisfies the following time-dependent Hamilton–Jacobi equation

$$\frac{\partial \varphi}{\partial t} + \mathbf{v} \cdot \nabla \varphi = 0, \qquad \mathbf{x} \in \mathbb{R}^3, \quad t \in \mathbb{R}^+, \tag{27}$$

with a suitable initial condition $\varphi(\mathbf{x}, 0) = \varphi_0(\mathbf{x})$ satisfying (26). If the vector field $\mathbf{v}$ always points in the direction normal to the surface, i.e. it has the form $\mathbf{v} = v\hat{\mathbf{n}}$, where $\hat{\mathbf{n}}$ is the unit exterior normal and v is some scalar function, the equation (27) turns into the time-dependent Eikonal equation

$$\frac{\partial \varphi}{\partial t} + v|\nabla \varphi| = 0, \qquad \mathbf{x} \in \mathbb{R}^3, \quad t \in \mathbb{R}^+. \tag{28}$$

This is indeed our case, since the drug particles dissolve in normal direction.

One of the most appealing features of the level-set method is that several geometrical properties of the evolving surface can be described by means of its level-set function φ. For example, it is possible to express the unit exterior normal $\hat{\mathbf{n}}$, the mean curvature κ_M, R, S and V in terms of φ and its derivatives [40]. More precisely, we have

$$\hat{\mathbf{n}} = \frac{\nabla \varphi}{|\nabla \varphi|}, \qquad \kappa_M = \operatorname{div} \hat{\mathbf{n}}, \qquad R = \frac{1}{\kappa_M}, \qquad S = \int_{\{\phi=0\}} ds, \qquad V = \int_{\{\phi<0\}} d\mathbf{x}. \tag{29}$$

Remark 2. Note that all the quantities introduced so far must be well defined everywhere in the space $\mathbb{R}^3$ and not only at the surface points (although they could have a clear physical meaning only there). This is a crucial fact for using the level-set method, since the evolution of the surface is actually replaced by the evolution of the level-set function φ, which is defined on the whole space and represents a sort of extension of the surface.

Tracking the particle dissolution

Reformulating (9) in the framework of the level-set method, we get that the evolution of the surface is described by the following dynamics:

$$\begin{cases} \dfrac{\partial \varphi}{\partial t} + v|\nabla \varphi| = 0 \\ v = -\dfrac{K[\varphi]}{\rho_s}\left(C_s - C_b\right) \\ \dfrac{dC_b}{dt} = \dfrac{C_s - C_b}{V_{\mathrm{EXT}}} \displaystyle\int_{\{\phi=0\}} K ds \end{cases}, \quad C_b < C_s, \tag{30}$$

with initial conditions given by (26) and $C_b(0) = 0$. In the previous equation, the symbol $K[\varphi]$ is used to denote the functional dependence of K on φ, since K is now evaluated using the whole function $\varphi : \mathbb{R}^3 \times \mathbb{R} \to \mathbb{R}$ and not only the pointwise values of the function φ at $(\mathbf{x}, t)$. When $C_b > C_s$ dissolution is stopped and recrystallization in the bulk fluid occurs:

$$\begin{cases} \dfrac{\partial \varphi}{\partial t} = 0 \\ \dfrac{dC_b}{dt} = \left(C_s - C_b\right) k_{rb} \end{cases}, \quad C_b \geq C_s.$$

If the particle dissolves completely, we can directly set $K = 0$ in (30).

Multiple particles

In the case of $N_P > 1$ particles dissolving in the same volume, one should track separately every particle. Differently from classical fields of application of the level-set method, here particles do not interact with each other: their dynamics are independent, but they all contribute to the concentration C_b by summing all single contributions. Therefore, in the presence of multiple particles the equation (30) is simply generalized by

$$\begin{cases} \dfrac{\partial \varphi_p}{\partial t} + v_p|\nabla \varphi_p| = 0 \\ v_p = -\dfrac{K_p[\varphi_p]}{\rho_s}\left(C_s - C_b\right) \\ \dfrac{dC_b}{dt} = \dfrac{C_s - C_b}{V_{\mathrm{EXT}}} \displaystyle\sum_{p=1}^{N_P} \int_{\{\varphi_p=0\}} K_p ds \end{cases}, \quad p = 1, \dots, N_P. \tag{31}$$

If we have $M > 1$ *identical* particles, one can avoid to track them separately. Indeed, their contribution to C_b will be obtained by simply multiplying the term $\int_{\{\varphi_p=0\}} K_p ds$ by M.

5. Numerical simulations

In this section we report the results of some numerical tests obtained by using the level-set methodology. As in [34], we prefer to work with a dimension-reduced 2D dynamics. This is done to simplify computations still allowing us to investigate qualitatively the impact of the particle shape and model's parameters on the dissolution dynamics. In particular, we expect that the behavior and role of corners is independent from the dimension. We also expect that, for axisymmetric shapes, all qualitative results about the time-dependent dissolution profile are preserved passing from 2D to 3D. Of course, results about particle's perimeter (respectively, area) in 2D must be transferred to its surface (respectively, volume) in 3D.

In Sect. 5.1, we consider the case of a single particle, for three drugs: theophylline (25 °C and 37 °C), griseofulvin (37 °C), and nimesulide (37 °C), with parameters as in Table 1. In particular, theophylline (25 °C) is considered to facilitate the comparison with results reported in [34]. These drugs are widely used in the pharmaceutical field [20] and they are representative of soluble and wettable drugs (theophylline), of poorly soluble but wettable drugs (griseofulvin), and of poorly soluble and poorly wettable drugs (nimesulide).

In Sect. 5.2, instead, the more realistic polydisperse case is analyzed, for griseofulvin (37 °C) only.

All numerical details are postponed to Appendix B.

5.1. Dissolution of a single particle

Test 1a: Circular particle (theophylline 25 °C)

In this preliminary test we consider a single circular particle of theophylline 25 °C with initial radius $R_0 = 50$ μm. The main goal here is to compare the result obtained by the level-set method with that reported in [34], as well as with the solution of the simplified problem detailed in Remark 1. Eq. (11) is solved using the third-order Runge-Kutta method and can be assumed to be the 'exact' solution.

Fig. 4 shows the evolution of the particle with $V^+ = 150$ and its level-set function φ, cut at the zero level set to get the particle's profile at a given time. In this case the recrystallization process is present. No appreciable difference can be seen comparing the

Table 1
Physical parameters used in numerical simulations.

Parameter	Symbol	Unit	Theoph. 25 °C	Theoph. 37 °C	Griseof. 37 °C	Nimes. 37 °C
Solid drug density	ρ_s	kg/m^3	1490	1490	1495	1476
Initial drug solubility	C_{s0}	kg/m^3	11.6	12.495	0.494	4.108
Final drug solubility	C_{sf}	kg/m^3	6.1	6.569	0.025	0.028
Surface recrystallization const.	k_r	s^{-1}	$6 \cdot 10^{-3}$	$6 \cdot 10^{-3}$	$8.8 \cdot 10^{-3}$	$1.3 \cdot 10^{-2}$
Bulk recrystallization const.	k_{rb}	s^{-1}	$6.6 \cdot 10^{-3}$	$5.7 \cdot 10^{-3}$	$8.36 \cdot 10^{-3}$	$1.235 \cdot 10^{-2}$
Interfacial flat mass transfer coeff.	k_m^∞	m/s	$3.7 \cdot 10^{-3}$	$2 \cdot 10^{-3}$	0.126	$1.8 \cdot 10^{-7}$
Drug diffusivity in water	D	m^2/s	$6.2 \cdot 10^{-10}$	$8.2 \cdot 10^{-10}$	$7.057 \cdot 10^{-10}$	$7.388 \cdot 10^{-10}$
Fluid density	ρ_f	kg/m^3	1000	993	993	993
Fluid dynamic viscosity	η_f	Pa s	10^{-3}	$6.91 \cdot 10^{-4}$	$6.91 \cdot 10^{-4}$	$6.91 \cdot 10^{-4}$
Fluid kinematic viscosity	ν_f	m^2/s	10^{-6}	$6.96 \cdot 10^{-7}$	$6.96 \cdot 10^{-7}$	$6.96 \cdot 10^{-7}$
Parameter in k_m	α	m^3	10^{-15}	10^{-15}	10^{-15}	10^{-15}
Tolman length	d_T	m	10^{-9}	$2.6 \cdot 10^{-10}$	$3.10 \cdot 10^{-10}$	$2.82 \cdot 10^{-10}$

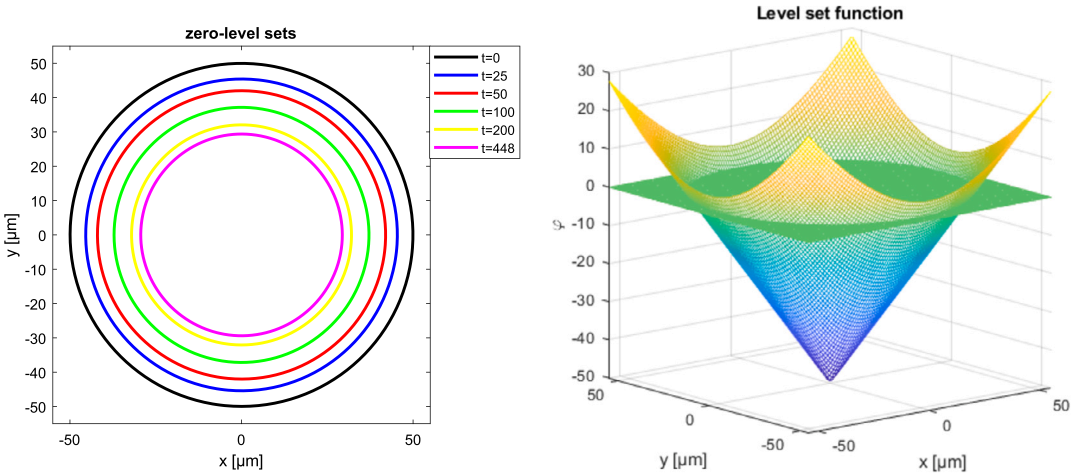

Fig. 4. Test 1a. Evolution of the particle with $V^+ = 150$ (left) and its level-set function φ (right). Time values are in seconds.

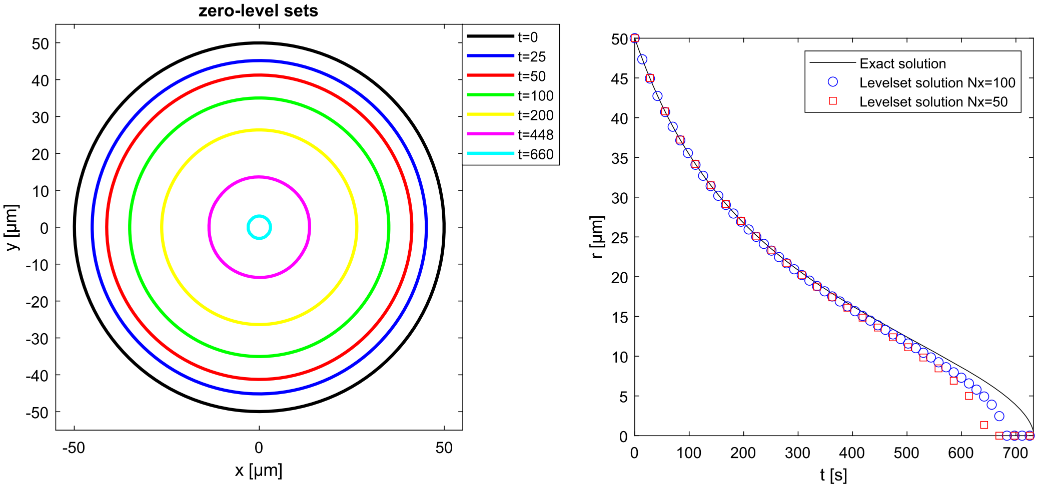

Fig. 5. Test 1a. Evolution of the particle with $V^+ = 300$ (left) and the evolution of the particle's radius $R(t)$ on a coarse/fine numerical grid (right). Time values are in seconds.

level-set solution with the results obtained in [34].

Fig. 5 reports the evolution of the particle with $V^+ = 300$ and the evolution of the particle's radius $R(t)$, comparing the exact solution and the level-set solution for two space steps Δx's (keeping the CFL ratio constant, see Appendix A). In this case the particle reaches the complete dissolution. Again, no significant difference is seen comparing the level-set solution with the results obtained in [34]. On the other hand, the level-set method does not catch very well the evolution of the particle when it is very small. This is

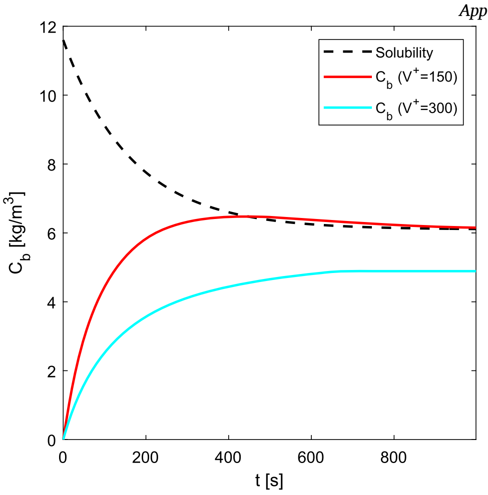

Fig. 6. Test 1a. Evolution of C_b for $V^+ = 150$ and $V^+ = 300$.

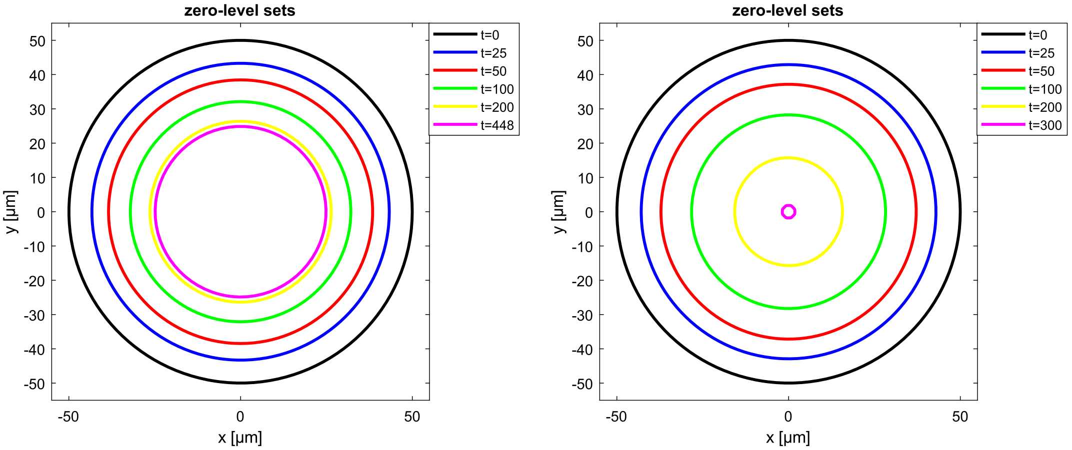

Fig. 7. Test 1b. Evolution of the particle with $V^+ = 150$ (left) and $V^+ = 300$ (right). Time values are in seconds.

due to the fact that the particle size becomes comparable with that of the grid cell. As expected, increasing the number of grid points (i.e. reducing Δx) the error diminishes.

Fig. 6 shows the curves of C_b for $V^+ = 150$ and $V^+ = 300$. It is interesting to underline that when the volume of the dissolution medium is large ($V^+ = 300$) recrystallization does not occur as drug concentration (blue line) never exceeds the time dependent drug solubility (dotted line). On the contrary, this event takes place for smaller V^+.

Test 1b: Circular particle (theophylline 37 °C)

To consider the effect of temperature, we consider now a single circular particle of theophylline at 37 °C with initial radius $R_0 = 50$ μm.

Fig. 7 (respectively, 8) shows the evolution of the particle surface (respectively, C_b) with $V^+ = 150$ and $V^+ = 300$. Comparison between Tests 1a and 1b reveals how the increase of temperature enhances the dissolution kinetics. This is due to the increased theophylline diffusion coefficient and solubility in the dissolution medium (water).

Test 2: From circle to square (theophylline 37 °C)

In this test we investigate the impact of the shape of a particle of theophylline on its evolution. We use superellipses (actually supercircles in this case), with exponent $2, 3, 39$ (see Appendix B.2 for details) in order to smoothly move from a circle to a square *with same initial areas* ($R_0 = 50$ μm for the circle and $V^+ = 150$).

Fig. 9 shows the dissolution profiles and the comparison of C_b's. We note that the sharp edges turn to become rounded, and the square tends to become a circle. Consequently the evolution of C_b is similar in the three cases. Both perimeter p and area A diminish in time. Their ratio p/A is also not constant, although the same trend for the three shapes is maintained, see Fig. 10. The highest values are reached by the square and the lowest by the circle.

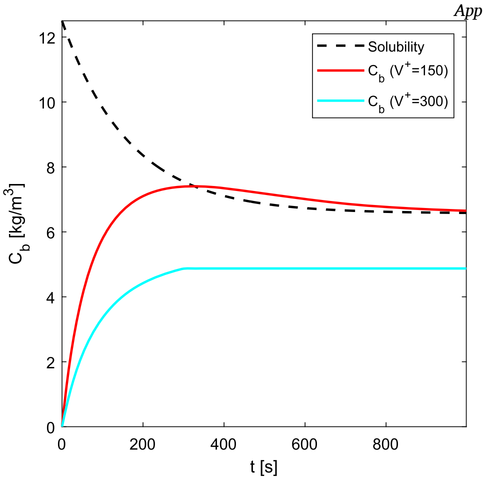

Fig. 8. Test 1b. Evolution of C_b for $V^+ = 150$ and $V^+ = 300$.

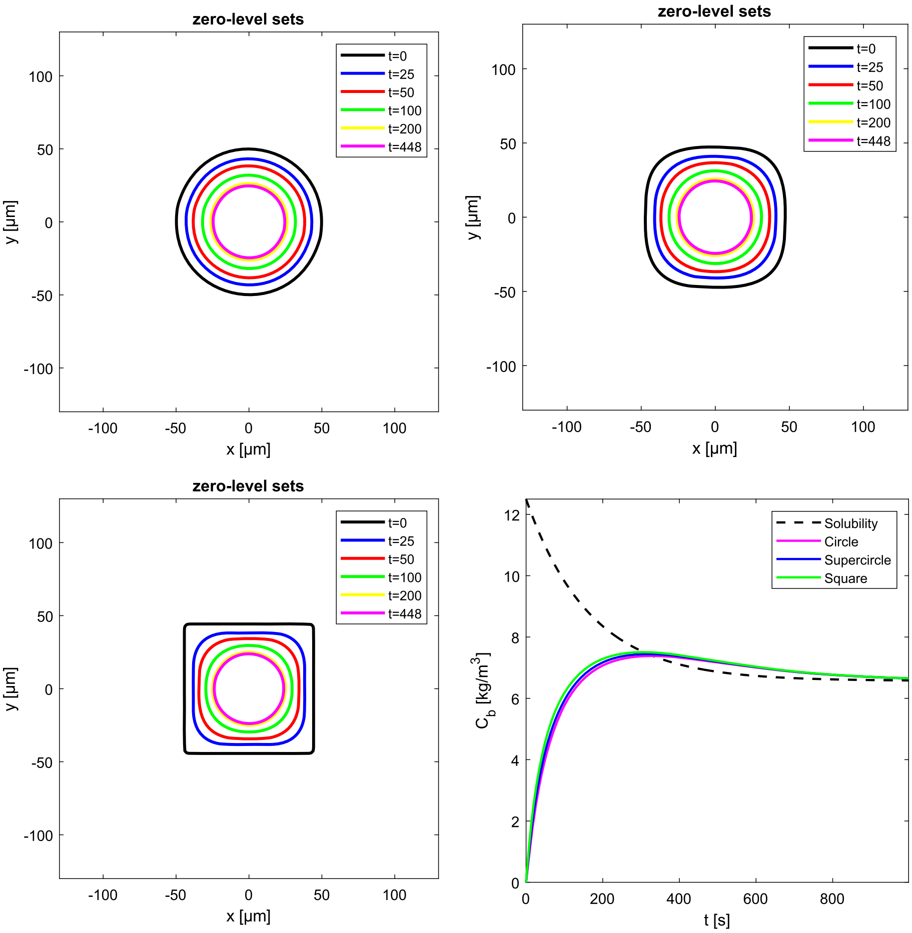

Fig. 9. Test 2. Dissolution profiles of particles with different initial shapes. Top-left: circle, top-right: supercircle ($n = 3$), bottom-left: square (actually a supercircle with $n = 39$). Bottom-right: evolution of C_b. Time values are in seconds.

Finally, Fig. 11 shows the mass transfer coefficient K at any point of the particle boundary, for the supercircle and the square. One can observe that K largely increases at corners, cf. [34].

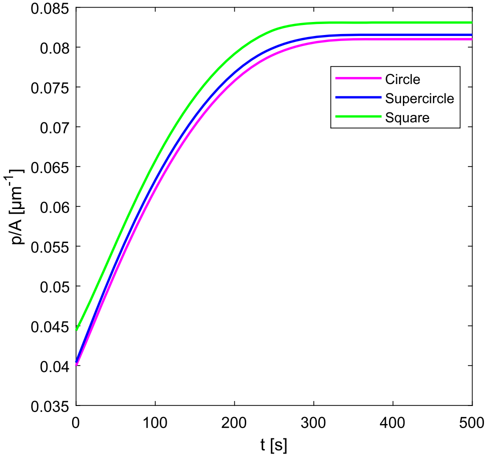

Fig. 10. Test 2. Evolution of p/A for the three shapes.

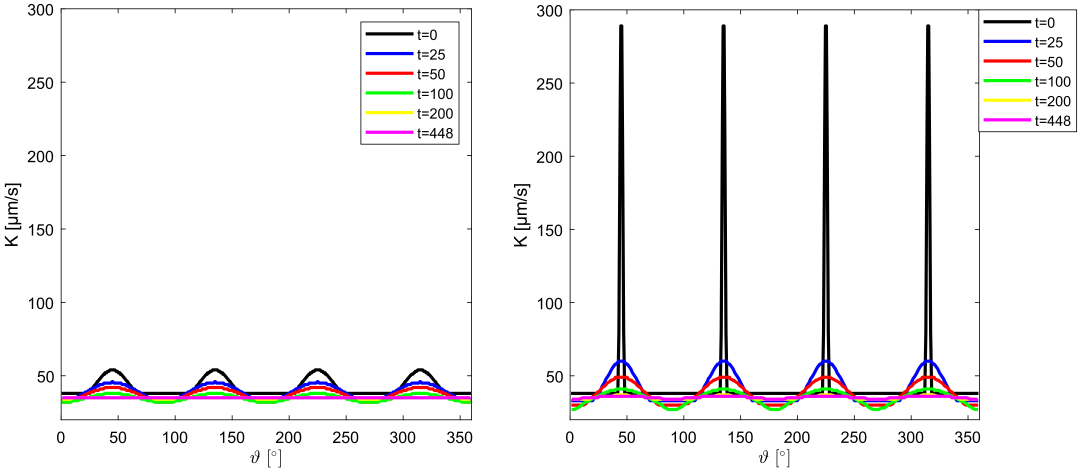

Fig. 11. Test 2. Mass transfer coefficient K as a function of the angle $\theta \in [0, 360°]$, at various times, for the supercircle ($n = 3$) (left) and the square (right). Time values are in seconds.

Test 3: From square to rectangle (theophylline 37 °C)

In this test we investigate further the impact of the shape of a particle of theophylline on its evolution using again superellipses with exponent $n = 39$, smoothly moving from a square to a rectangle of increasing aspect ratio, *with same initial areas* and $V^+ = 150$.

Fig. 12 shows the dissolution profiles and the comparison of C_b's. This time, the evolutions of C_b's are not similar, meaning that impact of the shape is not negligible.

Fig. 13 shows the evolution of the ratio p/A for the three shapes. The highest value is reached by the elongated rectangle and the lowest by the square. Here the difference among shapes is more significant than that observed in Fig. 10. This suggests that the evolution of C_b is influenced especially by the ratio p/A, rather than by the presence of corners. This evidence is very important from a practical point of view, as the reproducibility of dissolution experiments mainly depends on the particles' surface/volume ratio rather than on the presence of possible irregularities (corners) on particle surfaces.

Test 4: Irregular particles (theophylline 37 °C)

In this test we investigate how the proposed approach responds to irregularly-shaped particles, both smooth and sharpened. To this end, we consider two particles with the same area $A = 5{,}084.5\ \mu\text{m}^2$ ($R_{\text{EQ}} = 40.23\ \mu\text{m}$), and same $V^+ = 150$. Fig. 14 shows the dissolution profiles and the comparison of C_b's.

It can be seen that the corners immediately round, as already noted in the previous test. Also, the evolutions of C_b's are very similar, this is mainly due to the fact that the two profiles tend to have the same shape and area as the dissolution proceeds.

It is also worth noting that initially, and in both cases, some parts of the contours are flat or almost flat. This fact stresses the algorithm from the computational point of view, because of the swapping definition of k_d between (19) and (22). Nevertheless the computation is completed with no numerical artifacts.

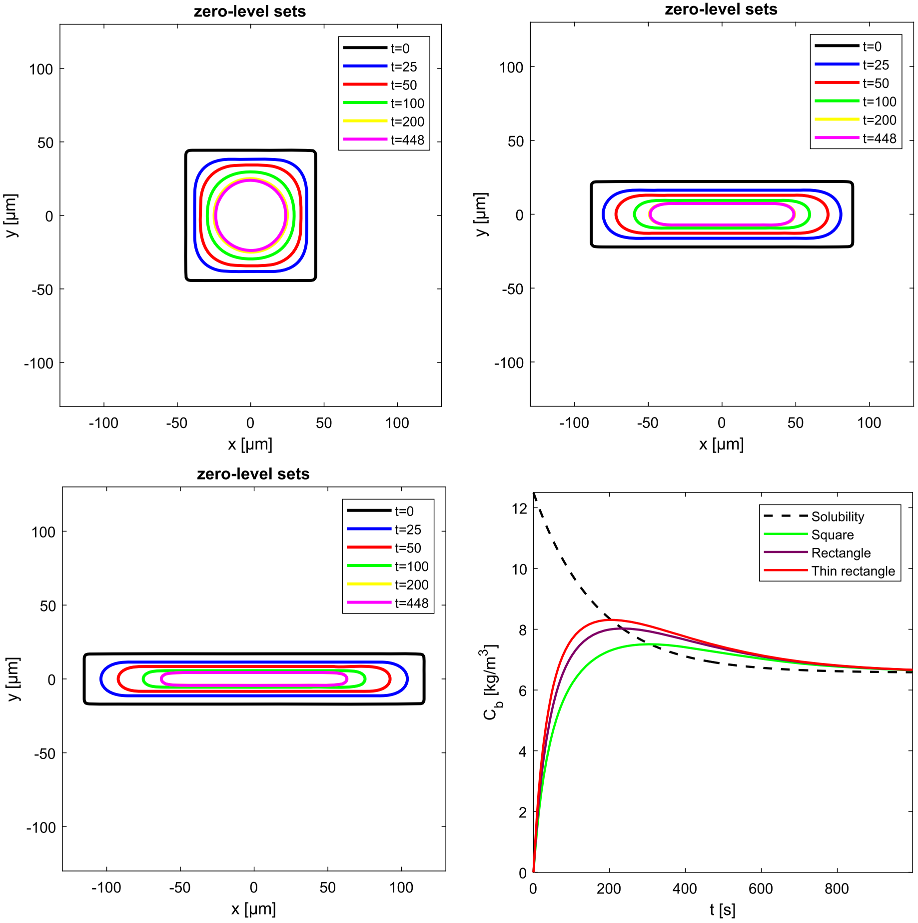

Fig. 12. Test 3. Dissolution profiles and comparison of C_b, for 3 rectangles with increasing aspect ratio. Initial dimensions are 87 µm × 87 µm (top-left), 177 µm × 44 µm (top-right), 231 µm × 34 µm (bottom-left). Time values are in seconds.

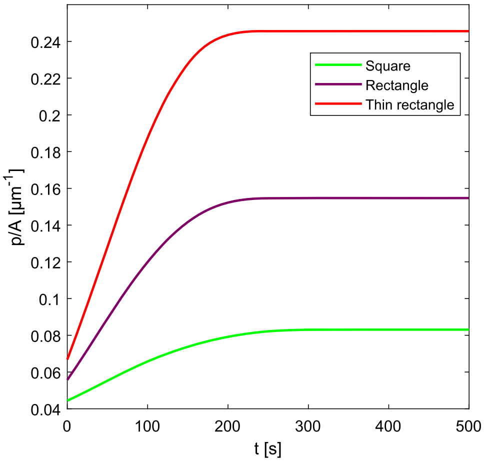

Fig. 13. Test 3. Evolution of the ratio p/A for the three shapes.

Test 5: Comparison between three drugs

Here we consider three circular particles of theophylline, griseofulvin and nimesulide (37 °C), all of them with initial radius $R_0 = 250$ µm and $V^+ = 150$. Even if such a radius is not physically feasible for all the three drugs, we perform this test to compare them all. Moreover, the value of C_b is normalized over C_{sf} for an effective comparison. Beside the comparison of the dissolution of the three drugs, we also aim at investigating the role of the parameter α appearing in (24) and ruling the interfacial mass transfer

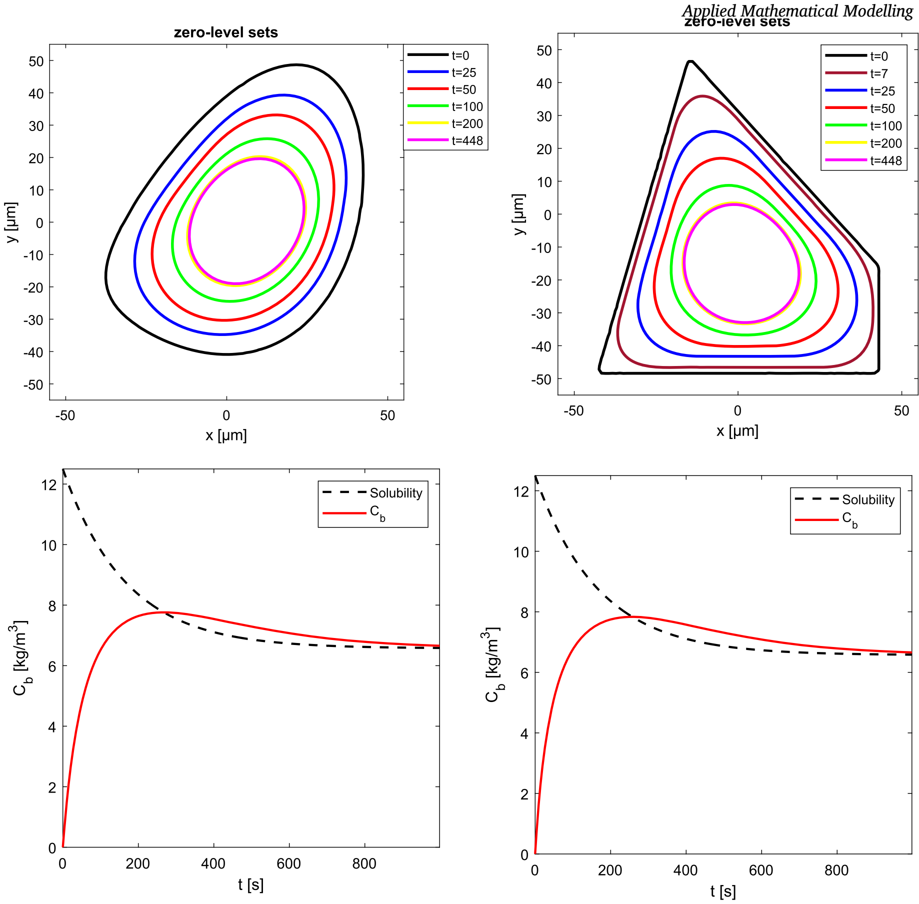

Fig. 14. Test 4. Dissolution profiles and comparison of C_b, for two irregularly-shaped particles. Smooth (left) and sharpened (right). Time values are in seconds.

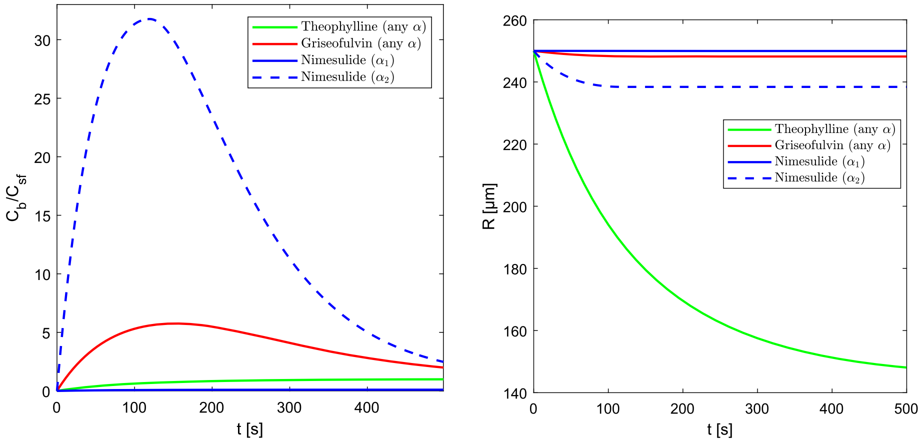

Fig. 15. Test 5. Evolution of C_b/C_{sf} (left) and evolution of the radii R (right) of circular particles of theophylline, griseofulvin, and nimesulide.

coefficient k_m, which is very difficult to measure experimentally. Therefore, we use *in silico* experiments to understand if it is possible to have a clue on α observing the particle's evolution *a posteriori*. To this goal, we use two values for α, i.e. $\alpha_1 = 10^{-15}$ and $\alpha_2 = 10^{-2}$.

Fig. 15 shows, for the three drugs, the evolution of C_b/C_{sf} and the evolution of the radii, with $\alpha = \alpha_1, \alpha_2$. It is observed that, among the three drugs, nimesulide is the only one for which α has a relevant impact on dissolution. This is not surprising as nimesulide is the only drug, among those considered, showing poor wettability, that is connected to an important role played by k_m on the dissolution kinetics.

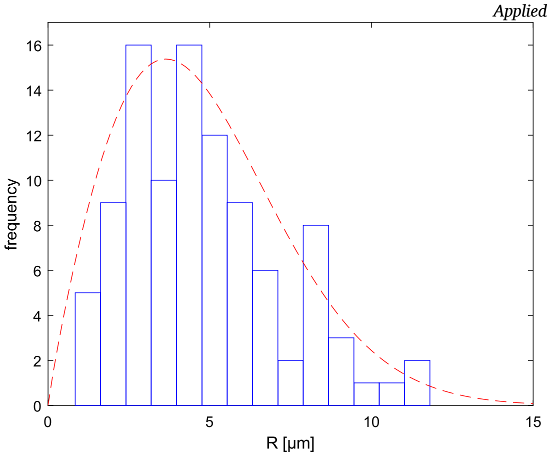

Fig. 16. Test 6. Particles' size (radius) distribution for 100 different circles (case c). Weibull distribution parameters: $\lambda = 5.4$, $k = 1.9$, $x_0 = 0$ [20, Fig. 1(a)]), see also Appendix A.

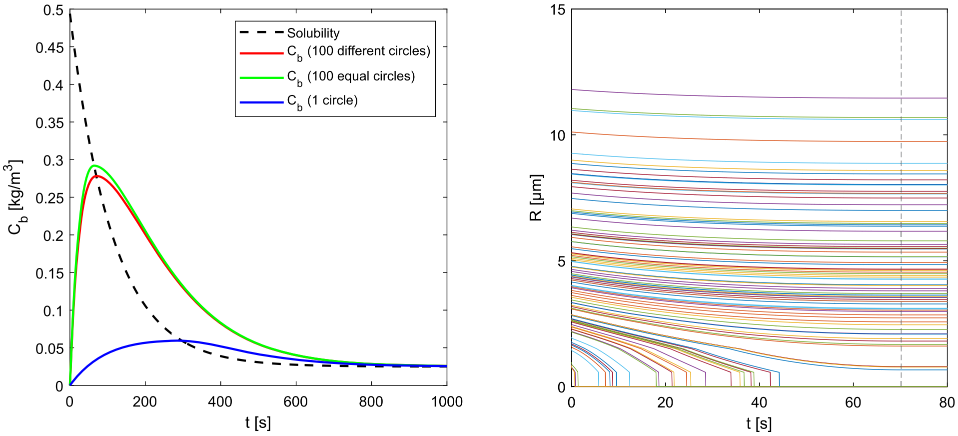

Fig. 17. Test 6. Evolution of C_b for cases a, b, c (left), and evolution of particles' radii for case c only (right). In case c, the 24 smallest particles reach full dissolution.

5.2. *Dissolution of multiple particles*

In the pharmaceutical experimental practice, drug powders and compounds appear smashed in a mixture of grains of different sizes and shapes, before being dissolved. In this section we analyze the effect of a polydisperse mixture of micro-sized particles in a variety of sizes and shapes.

In the following numerical tests we have chosen to work with griseofulvin (37 °C) because its particles' size range of a typical mixture is smaller (1-15 µm) [22,41] than those of the other considered drugs. This simplifies the numerical treatment because we can use the same numerical grid for all particles' sizes.

In the following we still denote by p and A the perimeter and the area of the particles, respectively, here meaning the *total* perimeter and the *total* area.

Test 6: Effect of the particles' size

In this test we compare the dissolution of three families of polydisperse drug particles sharing the same area ($A = 9,125.78$ µm^2), but having different perimeter p:

a) a single circular particle with initial radius $R_0 = 53.90$ µm ($p = 338.64$ µm);
b) 100 equal circular particles of initial radius $R_0 = 5.39$ µm ($p = 3,386.41$ µm);
c) 100 circular particles with different initial radii, randomly chosen according to the Weibull distribution, see Fig. 16 and Appendix A ($p = 3,019.70$ µm).

In all cases $V^+ = 1,000$. Fig. 17 shows that the single large particle (case a) and the 100 equal particles (case b) do not reach full dissolution, while the 24 smallest particles of case c undergo a full dissolution. As expected, C_b grows more rapidly in the case of many small particles, but the difference between cases b and c is mainly due to the different number of fully dissolved particles, rather than to the difference of p/A, cf. next test.

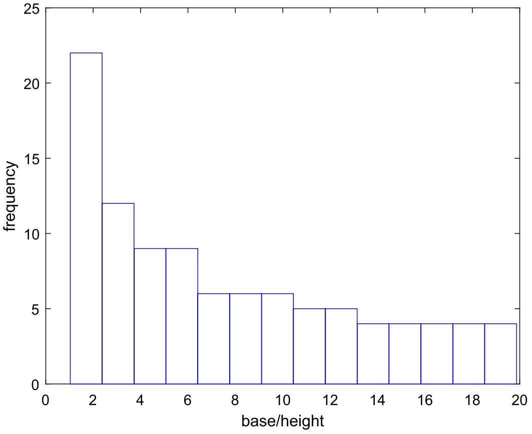

Fig. 18. Test 7. Rectangular particles' aspect ratio distribution.

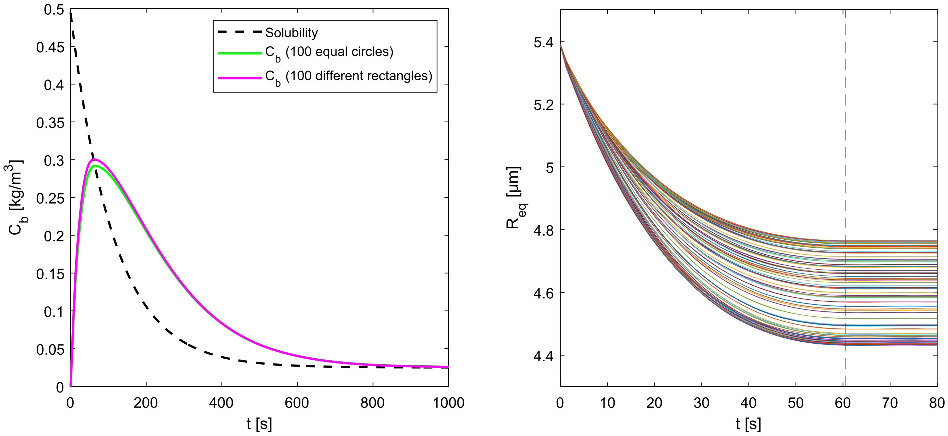

Fig. 19. Test 7. Left: Evolution of C_b for 100 equal circles (case b) and 100 rectangles (case d). Right: evolution of the 100 rectangles' equivalent radii. No particle reaches full dissolution.

Test 7: Effect of the particles' shape

To emphasize the influence of the shape, here two families of 100 particles, with the only difference in shape, are considered. The area of particles is the same, both individually as well as the total one. In particular, we compare the dissolution of 100 equal circular particles (case b of the previous test) with

d) 100 rectangular particles with different aspect ratios, with $p = 5,805.18$ μm, distributed as in Fig. 18.

We choose again $V^+ = 1,000$. Fig. 19 shows the evolution of C_b for case b and d, and the evolution of the rectangles' equivalent radii. Note that in this case no particle attains full dissolution. One can see here that the shape has a minor impact on the dissolution. Actually this is not in contrast with results of Test 3, for two reasons: griseofulvin is less sensitive to p/A and V^+ is relatively small to bring out a significant difference: for larger values of V^+ a more remarkable effect is indeed visible.

Test 8: The polydisperse case

To mimic a more realistic situation of a mixture with a variety of shape and sizes, in this final test the simultaneous dissolution of 20 circles, 50 ellipses, and 30 rectangles with randomly chosen size and aspect ratios, is simulated. We have $p = 6{,}117.06$ μm and $A = 48{,}814.13$ μm^2. The result is also compared with that of 61 equal circles of radius 15.96 μm, which share the same p and the same A with the mixture. Also, $V^+ = 10{,}000$.

Fig. 20 shows the evolution of C_b and that of the particles' equivalent radii. Results make it clear that particles shape and distribution (inside each shape) reflects in a small, but not negligible variation of the dissolution profile.

6. Conclusions

In order to understand the role played by the different concurrent phenomena taking place upon the dissolution of an ensemble of different particles (also referred to as DRT (Dissolution Rate Test [20]), this paper focuses on the realization of a mathematical model

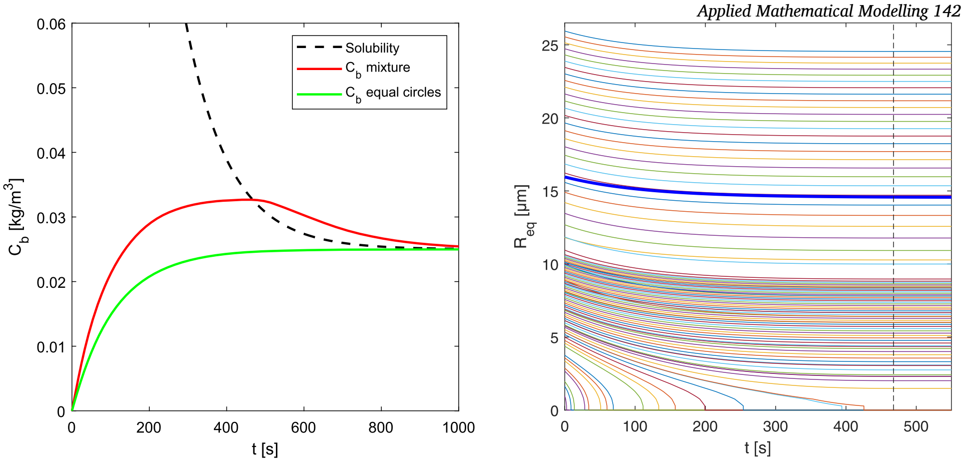

Fig. 20. Test 8. Left: evolution of C_b for 100 particles with different size and shape and 61 circles, same p and A. Right: evolution of the equivalent radii of the 100 particles with various shape an size (colored thin curves, 15 particles reach a full dissolution), and evolution of the radius of one of the 61 circular particles (blue thick curve).

able to consider the majority of them, with particular care devoted to particles shape, size distribution and surface properties. To this purpose, the three drugs (theophylline, griseofulvin and nimesulide), differing for shape, size distribution and for what concerns their water solubility and wettability, have been considered for the simulations of DRT. The numerical solution of the proposed model has been achieved by the level-set method [35], a reliable approach that has never been adopted before for the simulation of DRT and that is particular suitable to treat the presence of corners.

The main findings of our simulations reveal that, in general, the presence of corners appearing in the particle shape is not so important in determining the DRT kinetics. Indeed, due to the very high corner curvature (theoretically infinite), the local mass transport coefficient K is very high in comparison to that competing to the other parts of the surface. Thus, very rapidly, corners disappear and the particle shape tends to that of a sphere. This is the reason why, usually, the effect of corners on the whole dissolution phenomenon is not so relevant. Accordingly, our model makes it clear that the presence of small irregularities on particle surface should not matter so much in the theoretical interpretation of the DRT time course. On the other hand, particle shape is very important, with the particle surface/volume (S/V) ratio being one of the most important parameters. Indeed, the larger the value S/V, the faster the dissolution process occurs. In this sense, reasonably, we found a strict analogy between particle dissolution and particle melting [42]. Indeed, both dissolution and melting imply network destruction with the only difference that in the first case network breakdown is due to the external solvent, while in the second it is induced by temperature. Thus, increasing S/V – implying the enhancement of surface molecules number – promotes dissolution kinetics and reduces (nano) particle melting temperature.

Similarly, particles size distribution plays a very important role in ruling dissolution since, again, it is strictly connected to the S/V ratio, this time referring to all the particles and not to a specific one. Obviously, in real situations, the ensemble of dissolving particles is made up by particles of different shapes and different sizes. Interestingly, the developed model can account also for this real situation, so that it can safely simulate practical situations and it can be used to evaluate possible equivalence among particles ensembles characterized by particles of different shape and/or size distribution. Our simulations reveal that DRT kinetics not only depends on S/V but it also depends on particles shape and size distribution inside each shape, i.e. the situation met in real situations. Clearly, this is very important in the light of quality control that resorts to DRT to establish equivalence among different particles lots. At the same time, the model can be used to study some important surface properties such as the presence of a surface phase, differing from the bulk one, and induced by dissolution (surface recrystallization). In addition, the proposed model accounts also for solid wettability providing an important generalization of the expression of the interfacial mass transfer coefficient k_m [34].

Finally, we do believe that the proposed model represents a very important theoretical tool to interpret the experimental evidence coming from the developing experimental set up aimed to visualize particle shape variation upon dissolution [26,43,44]. This, clearly, will imply to move from a two-dimensional model to a three-dimensional one.

CRediT authorship contribution statement

Emiliano Cristiani: Writing – review & editing, Writing – original draft, Supervision, Software, Methodology, Investigation, Formal analysis. **Mario Grassi:** Writing – review & editing, Writing – original draft, Supervision, Methodology, Investigation, Formal analysis, Conceptualization. **Francesca L. Ignoto:** Writing – review & editing, Software, Methodology, Investigation, Formal analysis. **Giuseppe Pontrelli:** Writing – review & editing, Writing – original draft, Supervision, Methodology, Investigation, Formal analysis, Conceptualization.

Funding

E.C. and F.L.I. was funded by INdAM–GNCS Project entitled "Numerical modeling and high-performance computing approaches for multiscale models of complex systems" (PI: M. Menci), CUP E53C23001670001.

Declaration of competing interest

The authors declare that they have no known competing financial interests or personal relationships that could have appeared to influence the work reported in this paper.

Acknowledgements

E.C., F.L.I., and G.P. are members of the INdAM–GNCS research group.

Appendix A. Particle distribution

It is known that the size of the solid drug particles is randomly distributed following shifted Weibull distribution [20]

$$f(x) = \frac{k}{\lambda^k}(x - x_0)^{k-1} \exp\left[-\left(\frac{x - x_0}{\lambda}\right)^k\right], \qquad x > x_0. \tag{32}$$

In this case, the cumulative distribution is given by

$$F(x) = \int_{-\infty}^{x} f(\zeta)d\zeta = 1 - \exp\left[-\left(\frac{x - x_0}{\lambda}\right)^k\right], \qquad x > x_0, \tag{33}$$

and the inverse of F is given by

$$Q(y) = \lambda(-\ln(1 - y))^{\frac{1}{k}} + x_0, \quad y \in [0, 1]. \tag{34}$$

Using (34) one can easily extract any number n of random samples $R_1, \dots, R_n$ distributed accordingly to (32), simply defining

$$R_i = Q(y_i), \qquad i = 1, \dots, n,$$

with y_i *uniformly* random variables in [0,1].

Appendix B. Numerical discretization

In this Appendix we describe in full details the numerical method we used to obtain the simulations of Section 5.

B.1. Numerical grid and CFL condition

Let us introduce a structured grid $\mathcal{G}$. We consider a square computational domain divided in $N \times N$ square cells of side Δx. Let us denote as usual by x_{ij} the grid node corresponding to the point $(i\Delta x, j\Delta x)$, and by C_{ij} the cell with vertices $(x_{ij}, x_{i+1,j}, x_{i,j+1}, x_{i+1,j+1})$.

Regarding time discretization, let us denote by Δt the time step and by $t^n = n\Delta t$ the physical time at the n-th time step.

A crucial observation regards the CFL condition: indeed, such differential problems involving hyperbolic partial differential equations like (28) require the ratio between time and space steps being chosen in such a way that

$$\frac{\Delta t}{\Delta x} \leq \frac{1}{\max_{\mathcal{G}} |v_{ij}|}. \tag{35}$$

This guarantees the numerical stability.

B.2. Shape initialization (computation of φ_0)

Computing the initial condition φ_0 for the level-set function (under constraint (26)) is a problem *per se*. The difficulty is increased by the fact that the accuracy of the following evolution of φ strongly depends on the accuracy of the initial condition φ_0. A typical choice for φ_0 is the *signed distance function* from the initial curve. To begin with, let us recall the equations in polar coordinates of the curves we have considered:

$$\begin{array}{lll} \textit{circle} & r(\theta) = R, & \theta \in [0, 2\pi), \\ \textit{superellipse} & r(\theta) = \left(\left|\frac{\cos\theta}{a}\right|^n + \left|\frac{\sin\theta}{b}\right|^n\right)^{-1/n}, & \theta \in [0, 2\pi),\ n \geq 2 \text{ (ellipse with } n = 2). \end{array}$$

Once we have this, we can easily get the points of the initial curves with arbitrary accuracy. Then, for any grid node, we can compute the distance between the node and the curve by finding the minimal distance between the node and any point of the curve. This step is relatively expensive but it must be done only once. The last step requires to discriminate if the point is internal or external. This can be done by solving the well known point-in-polygon problem using, e.g., the ray casting algorithm or the winding number algorithm.

B.3. Numerical scheme for the level-set equation

Here we recall the first-order upwind numerical scheme we have used to solve (28) in two dimension [40, Sect. 6.4]. As usual we denote by φ^n_{ij} the approximation of the level-set function φ at the grid node $(i\Delta x, j\Delta x)$ and time $n\Delta t$. Similarly for v^n_{ij}.

The scheme reads as

$$\varphi^{n+1}_{ij} = \varphi^n_{ij} - \Delta t \left(\max(v^n_{ij}, 0)\Lambda^n_+ + \min(v^n_{ij}, 0)\Lambda^n_- \right), \qquad \forall i, j, n > 0$$

with

$$\Lambda^n_+ := \sqrt{\max(D^-_x \varphi^n_{ij}, 0)^2 + \min(D^+_x \varphi^n_{ij}, 0)^2 + \max(D^-_y \varphi^n_{ij}, 0)^2 + \min(D^+_y \varphi^n_{ij}, 0)^2}$$

$$\Lambda^n_- := \sqrt{\max(D^+_x \varphi^n_{ij}, 0)^2 + \min(D^-_x \varphi^n_{ij}, 0)^2 + \max(D^+_y \varphi^n_{ij}, 0)^2 + \min(D^-_y \varphi^n_{ij}, 0)^2}$$

and

$$D^+_x \varphi^n_{ij} := \frac{\varphi^n_{i+1,j} - \varphi^n_{ij}}{\Delta x}, \qquad D^-_x \varphi^n_{ij} := \frac{\varphi^n_{ij} - \varphi^n_{i-1,j}}{\Delta x},$$

$$D^+_y \varphi^n_{ij} := \frac{\varphi^n_{i,j+1} - \varphi^n_{ij}}{\Delta x}, \qquad D^-_y \varphi^n_{ij} := \frac{\varphi^n_{ij} - \varphi^n_{i,j-1}}{\Delta x}.$$

B.4. Computation of R

Let us recall from Sect. 3 that R is the inverse of the curvature. In 2D, for any x, y, the curvature can be written in terms of the level-set function using the formula [40],

$$\kappa = \frac{\varphi_{xx}\varphi_y^2 - 2\varphi_x\varphi_y\varphi_{xy} + \varphi_{yy}\varphi_x^2}{(\varphi_x^2 + \varphi_y^2)^{3/2}}.$$

The derivatives of φ can be approximated, e.g., by centered finite differences,

$$\varphi_x \approx \frac{\varphi_{i+1,j} - \varphi_{i-1,j}}{2\Delta x}, \qquad \varphi_y \approx \frac{\varphi_{i,j+1} - \varphi_{i,j-1}}{2\Delta x}$$

$$\varphi_{xx} \approx \frac{\varphi_{i+1,j} - 2\varphi_{i,j} + \varphi_{i-1,j}}{\Delta x^2}, \qquad \varphi_{yy} \approx \frac{\varphi_{i,j+1} - 2\varphi_{i,j} + \varphi_{i,j-1}}{\Delta x^2},$$

$$\varphi_{xy} \approx \frac{\varphi_{i+1,j+1} - \varphi_{i+1,j-1} - \varphi_{i-1,j+1} + \varphi_{i-1,j-1}}{4\Delta x^2}.$$

B.5. Computation of perimeter and area of the particle

One of the most technical steps in the numerical approximation of the level-set equation (30) is the computation of the perimeter and the area of the particle, which are needed to evaluate R_{EQ} and then $\int_{\varphi=0} K ds$ by a quadrature formula, at any time step.

The goal here is to locate the boundary of the particle by means of the level-set function φ. This can be done noting that the boundary divides the space in two regions, characterized by $\varphi > 0$ (the exterior) and $\varphi < 0$ (the interior). The grid cells which are crossed by the boundary are easily found since the values of φ at their four vertices have different sign. By interpolation (we use linear) one can locate one point, say $\mathbf{q}_1$, of the boundary passing through a side of a grid cell, see Fig. 21.

Once the first point is found, it is labeled as “incoming” in a cell (cell C_1 in Fig. 21). Then, by comparing the signs of φ along the vertices of the cell, one can search for the “outgoing” point $\mathbf{q}_2$ (which corresponds to the incoming point in the next cell C_2). Repeating the procedure one can move from one cell to another until the first point is reached again. At this point the perimeter is easily computed by summing all the lengths of the lines joining one point with the following one, i.e. $\sum_{i=1}^{n-1} \|\mathbf{q}_{i+1} - \mathbf{q}_i\|$.

Regarding the area, the cells fully inside the particle are easily found, being characterized by having $\varphi < 0$ at the four vertices. In order to increase the accuracy, one can add to the areas of the fully contained cells, the areas of the internal part of the cells crossed by the particle boundary (red areas in the Figure).

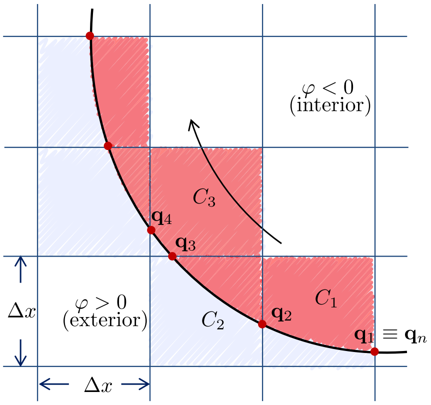

Fig. 21. Localization of the boundary of a particle on the grid.

Appendix C. Derivation of k_m

The theoretical dependence of the mass transport coefficient k_m on the local curvature radius R can be evaluated resorting to the estimation of the infinitesimal variation of the internal energy U competing to the interface separating the solid and the solution phases [45]:

$$dU = TdS + \sum_{i=1}^{r} \mu_i dn_i + \gamma dA + C_1 d\kappa_1 + C_2 d\kappa_2, \tag{36}$$

where – limited to this Appendix – r is the number of mixture components, T and S denote, respectively, the interface temperature and entropy, while μ_i and n_i are, respectively, the interface chemical potential and the moles number associated to the ith species. γ and A denote, respectively, the interface surface energy and area, while κ_1 and κ_2 represent, respectively, the first and the second interface curvature, being C_1 and C_2 two constants.

Dividing (36) by dA and remembering that only two species can exist (1 = solid; 2 = solvent), we have:

$$\frac{\partial U}{\partial A} = T\frac{\partial S}{\partial A} + \mu_1 \frac{\partial n_1}{\partial A} + \mu_2 \frac{\partial n_2}{\partial A} + \gamma + C_1 \frac{\partial \kappa_1}{\partial A} + C_2 \frac{\partial \kappa_2}{\partial A}. \tag{37}$$

As S and n_i are extensive functions of A and increase linearly with A, we can set:

$$\frac{\partial S}{\partial A} = k_S, \qquad \frac{\partial n_1}{\partial A} = k_{n_1}, \qquad \frac{\partial n_2}{\partial A} = k_{n_2}. \tag{38}$$

On the basis of (38) and assuming that n_2 is negligible in comparison to n_1 (this assumption relies on the usual hypothesis that the liquid phase does not pervade the solid one in a solid-liquid equilibrium), (37) becomes:

$$\frac{\partial U}{\partial A} \approx Tk_S + \mu_1 k_{n_1} + \gamma + C_1 \frac{\partial \kappa_1}{\partial A} + C_2 \frac{\partial \kappa_2}{\partial A}. \tag{39}$$

If we further suppose that $\kappa_1 \approx \kappa_2$ (we locally approximate the surface by a sphere), it follows:

$$\frac{\partial \kappa_1}{\partial A} \approx \frac{\partial \kappa_2}{\partial A} = \frac{\partial\left(\frac{1}{R}\right)}{\partial(4\pi R^2)} = -\frac{1}{8\pi R^3}. \tag{40}$$

Inserting (40) into (39) leads to:

$$\frac{\partial U}{\partial A} \approx Tk_S + \mu_1 k_{n_1} + \gamma - \frac{(C_1 + C_2)}{8\pi R^3}. \tag{41}$$

As equilibrium conditions require $dU = 0$, we have:

$$Tk_S + \mu_1 k_{n_1} + \gamma - \frac{(C_1 + C_2)}{8\pi R^3} = 0. \tag{42}$$

Solving (42) for μ_1 leads to:

$$\mu_1 = \frac{(C_1 + C_2)}{8\pi k_{n_1}} \frac{1}{R^3} - \frac{\gamma}{k_{n_1}} - \frac{Tk_S}{k_{n_1}}. \tag{43}$$

In the light of the Tolman equation [46]:

$$\gamma = \gamma_\infty \frac{R}{R + 2d_T} \tag{44}$$

where γ_∞ is the solid-liquid surface energy for a flat surface (vanishing curvature) and d_T is the Tolman length, whose order of magnitude should correspond to the diameter of the molecules constituting the curved surface [47], but it is usually assumed to be 1/3 of the molecules diameter [48], (43) becomes:

$$\mu_1 = \frac{(C_1 + C_2)}{8\pi k_{n_1}} \frac{1}{R^3} - \frac{\gamma_\infty}{k_{n_1}} \frac{R}{R + 2d_T} - \frac{T k_S}{k_{n_1}}. \tag{45}$$

As the chemical potential expresses the tendency of solid surface molecules to leave the interface, we can argue that k_m is proportional to μ_1. Assuming that k_m gets its minimum value (that corresponding to a plane surface, $R \to \infty$) when $\mu_1 = 0$, (45) seems to suggest that a reasonable k_m dependence on R is given by:

$$k_m = k_m^\infty \left(\frac{\alpha}{R^3} + \frac{R}{R + 2d_T} \right) \tag{46}$$

where α is an unknown parameter to be determined.

Data availability

No data was used for the research described in the article.

References

[1] J. Siepmann, F. Siepmann, Mathematical modeling of drug dissolution, Int. J. Pharm. 453 (1) (2013) 12–24.
[2] D. Hasa, B. Perissutti, D. Voinovich, M. Abrami, R. Farra, S.M. Fiorentino, G. Grassi, M. Grassi, Drug nanocrystals: theoretical background of solubility increase and dissolution rate enhancement, Chem. Biochem. Eng. Q. 28 (3) (2014) 247–258.
[3] A. Parmar, S. Sharma, Engineering design and mechanistic mathematical models: standpoint on cutting edge drug delivery, TrAC, Trends Anal. Chem. 100 (2018) 15–35.
[4] K.C. Kwan, Oral bioavailability and first-pass effects, Drug Metab. Dispos. 25 (12) (1997) 1329–1336.
[5] R. Naidu, K.T. Semple, M. Megharaj, A.L. Juhasz, N.S. Bolan, S.K. Gupta, B.E. Clothier, R. Schulin, Bioavailability: definition, assessment and implications for risk assessment, Dev. Plant Soil Sci. 32 (2008) 39–51.
[6] T. Loftsson, M.E. Brewster, Pharmaceutical applications of cyclodextrins: basic science and product development, J. Pharm. Pharmacol. 62 (11) (2010) 1607–1621.
[7] M. Davis, G. Walker, Recent strategies in spray drying for the enhanced bioavailability of poorly water-soluble drugs, J. Control. Release 269 (2018) 110–127.
[8] M.R. Gigliobianco, C. Casadidio, R. Censi, P. Di Martino, Nanocrystals of poorly soluble drugs: drug bioavailability and physicochemical stability, Pharmaceutics 10 (3) (2018) 134.
[9] S. Bertoni, B. Albertini, N. Passerini, Spray congealing: an emerging technology to prepare solid dispersions with enhanced oral bioavailability of poorly water soluble drugs, Molecules 24 (19) (2019) 3471.
[10] A.W. Hixson, J.H. Crowell, Dependence of reaction velocity upon surface and agitation I. Theoretical consideration, Ind. Eng. Chem. 23 (8) (1931) 923–931.
[11] A.W. Hixson, J.H. Crowell, Dependence of reaction velocity upon surface and agitation II. Experimental procedure in study of surface, Ind. Eng. Chem. 23 (9) (1931) 1002–1009.
[12] A.W. Hixson, J.H. Crowell, Dependence of reaction velocity upon surface and agitation III. Experimental procedure in study of agitation, Ind. Eng. Chem. 23 (10) (1931) 1160–1169.
[13] P.J. Niebergall, G. Milosovich, J.E. Goyan, Dissolution rate studies II: dissolution of particles under conditions of rapid agitation, J. Pharm. Sci. 52 (3) (1963) 236–241.
[14] P.V. Pedersen, K.F. Brown, Dissolution profile in relation to initial particle distribution, J. Pharm. Sci. 64 (7) (1975) 1192–1195.
[15] P.V. Pedersen, K.F. Brown, Size distribution effects in multiparticulate dissolution, J. Pharm. Sci. 64 (12) (1975) 1981–1986.
[16] P.V. Pedersen, K.F. Brown, General class of multiparticulate dissolution models, J. Pharm. Sci. 66 (10) (1977) 1435–1438.
[17] P.V. Pedersen, J.W. Myrick, Versatile kinetic approach to analysis of dissolution data, J. Pharm. Sci. 67 (10) (1978) 1450–1455.
[18] M. Grassi, G. Grassi, R. Lapasin, I. Colombo, Understanding Drug Release and Absorption Mechanisms: A Physical and Mathematical Approach, CRC Press, Boca Raton, USA, 2007.
[19] N. Guo, B. Hou, N. Wang, Y. Xiao, J. Huang, Y. Guo, S. Zong, H. Hao, In situ monitoring and modeling of the solution-mediated polymorphic transformation of rifampicin: from form II to form I, J. Pharm. Sci. 107 (1) (2018) 344–352.
[20] M. Abrami, L. Grassi, R. Di Vittorio, D. Hasa, B. Perissutti, D. Voinovich, G. Grassi, I. Colombo, M. Grassi, Dissolution of an ensemble of differently shaped poly-dispersed drug particles undergoing solubility reduction: mathematical modelling, ADMET DMPK 8 (3) (2020) 297–313.
[21] U. Thormann, M. De Mieri, M. Neuburger, S. Verjee, P. Altmann, M. Hamburger, G. Imanidis, Mechanism of chemical degradation and determination of solubility by kinetic modeling of the highly unstable sesquiterpene lactone nobilin in different media, J. Pharm. Sci. 103 (10) (2014) 3139–3152.
[22] M. Mosharraf, C. Nyström, The effect of particle size and shape on the surface specific dissolution rate of microsized practically insoluble drugs, Int. J. Pharm. 122 (1–2) (1995) 35–47.
[23] D. Hirai, Y. Iwao, S.-I. Kimura, S. Noguchi, S. Itai, Mathematical model to analyze the dissolution behavior of metastable crystals or amorphous drug accompanied with a solid-liquid interface reaction, Int. J. Pharm. 522 (1–2) (2017) 58–65.
[24] S.-Y. Hsu, C.-W. Wu, Effects of particle shape in mass-diffusion-controlled dissolution process, Int. Commun. Heat Mass Transf. 125 (2021) 105321.
[25] Q. Yuan, X. Jia, R.A. Williams, Validation of a multi-component digital dissolution model for irregular particles, Powder Technol. 240 (2013) 25–30.
[26] M. Lausch, P. Brockmann, F. Schmitt, B.J.M. Etzold, J. Hussong, In-situ iron oxide particle size and shape evolution during the dissolution in oxalic acid, Chem. Eng. Sci. 289 (2024) 119864.
[27] J.-P. Hsu, D.-L. Lin, M.-J. Lin, Dissolution of solid particles in liquids: a surface layer model, Colloids Surf. 61 (1991) 35–47.
[28] J. Wang, D.R. Flanagan, General solution for diffusion-controlled dissolution of spherical particles. 1. Theory, J. Pharm. Sci. 88 (7) (1999) 731–738.
[29] K. Salish, C. So, S.H. Jeong, H.H. Hou, C. Mao, A refined thin-film model for drug dissolution considering radial diffusion – simulating powder dissolution, Pharm. Res. 41 (2024) 947–958.
[30] D.M. D'Arcy, T. Persoons, Mechanistic modelling and mechanistic monitoring: simulation and shadowgraph imaging of particulate dissolution in the flow-through apparatus, J. Pharm. Sci. 100 (3) (2011) 1102–1115.
[31] D.M. D'Arcy, T. Persoons, Understanding the potential for dissolution simulation to explore the effects of medium viscosity on particulate dissolution, AAPS PharmSciTech 20 (2019) 47.
[32] M. Assunção, M. Vynnycky, K.M. Moroney, On the dissolution of a solid spherical particle, Phys. Fluids 35 (2023) 053605.

[33] M. Assunção, M. Vynnycky, K.M. Moroney, Free-convective dissolution of a solid spherical particle, Phys. Fluids 36 (2024) 043604.
[34] M. Abrami, M. Grassi, D. Masiello, G. Pontrelli, Dissolution of irregularly-shaped drug particles: mathematical modelling, Eur. J. Pharm. Biopharm. 177 (2022) 199–210.
[35] S. Osher, J.A. Sethian, Front propagating with curvature-dependent speed: algorithms based on Hamilton-Jacobi formulations, J. Comput. Phys. 79 (1) (1988) 12–49.
[36] H. Nogami, T. Nagai, T. Yotsuyanagi, Dissolution phenomena of organic medicinals involving simultaneous phase changes, Chem. Pharm. Bull. 17 (3) (1969) 499–509.
[37] V.G. Levich, Physicochemical Hydrodynamics, Prentice-Hall, Englewood Cliffs, N.J., 1962.
[38] W.E. Ranz, W.R. Marshall, Evaporation from drops, Chem. Eng. Prog. 48 (1952) 41–146.
[39] S. Osher, R. Fedkiw, Level Set Methods and Dynamic Implicit Surfaces, Applied Mathematical Sciences., vol. 153, Springer-Verlag, New York, 2003.
[40] J.A. Sethian, Level Set Methods and Fast Marching Methods: Evolving Interfaces in Computational Geometry Fluid Mechanics, Computer Vision, and Material Science, Cambridge University Press, New York, 1999.
[41] A. Naseem, C.J. Olliff, L.G. Martini, A.W. Lloyd, Effects of plasma irradiation on the wettability and dissolution of compacts of griseofulvin, Int. J. Pharm. 269 (2) (2004) 443–450.
[42] G. Chiarappa, A. Piccolo, I. Colombo, D. Hasa, D. Voinovich, M. Moneghini, G. Grassi, R. Farra, M. Abrami, P. Posocco, S. Prici, M. Grassi, Exploring the shape influence on melting temperature, enthalpy, and solubility of organic drug nanocrystals by a thermodynamic model, Cryst. Growth Des. 17 (8) (2017) 4072–4083.
[43] R. Laitinen, J. Lahtinen, P. Silfsten, E. Vartiainen, P. Jarho, J. Ketolainen, An optical method for continuous monitoring of the dissolution rate of pharmaceutical powders, J. Pharm. Biomed. Anal. 52 (2) (2010) 181–189.
[44] J. Štukelj, M. Agopov, J. Yliruusi, C.J. Strachan, S. Svanbäck, Image-based dissolution analysis for tracking the surface stability of amorphous powders, ADMET DMPK 8 (4) (2020) 401–409.
[45] A.W. Adamson, A.P. Gast, Physical Chemistry of Surfaces, Wiley, New York, 1997.
[46] R.C. Tolman, The effect of droplet size on surface tension, J. Chem. Phys. 17 (3) (1949) 333–337.
[47] V.M. Samsonov, N.Y. Sdobnyakov, A.N. Bazulev, Size dependence of the surface tension and the problem of Gibbs thermodynamics extension to nanosystems, Colloids Surf. A, Physicochem. Eng. Asp. 239 (1–3) (2004) 113–117.
[48] J.S. Rowlinson, B. Widom, Molecular Theory of Capillarity, Clarendon Press, Oxford, 1982.